


Multiple magnetoelectric plateaus in the polar magnet $\text{Fe}_2\text{Mo}_3\text{O}_8$

Qian Chen ¹, Atsushi Miyake,¹ Takashi Kurumaji,² Keisuke Matsuura,³ Fumitaka Kagawa,^{3,4} Shin Miyahara,⁵ Yoshinori Tokura,^{3,6} and Masashi Tokunaga¹

¹*Institute for Solid State Physics, The University of Tokyo, Kashiwa, Chiba 277-8581, Japan*

²*Department of Advanced Materials Science, The University of Tokyo, Kashiwa 277-8561, Japan*

³*RIKEN Center for Emergent Matter Science, Wako 351-0198, Japan*

⁴*Department of Physics, Tokyo Institute of Technology, Tokyo 152-8551, Japan*

⁵*Department of Applied Physics, Fukuoka University, Jonan-ku, Fukuoka 814-0180, Japan*

⁶*Tokyo College and Department of Applied Physics, The University of Tokyo, Hongo, Tokyo 113-8656, Japan*



(Received 6 September 2023; accepted 20 February 2024; published 12 March 2024)

The magnetization and electric polarization of a polar antiferromagnet $\text{Fe}_2\text{Mo}_3\text{O}_8$ are studied up to 66 T for spin-saturation magnetic fields applied along the polar axis. The magnetization process at 1.4 K exhibited an unusual six-step structure below the saturation field of 65 T, which has scarcely been observed in frustrated magnets. The electric polarization along the polar axis exhibits a similar multistep behavior with a total change of $1.2 \mu\text{C}/\text{cm}^2$. A combined triangular-lattice antiferromagnetic model with strong Ising-type spin anisotropy reproduces this multistep magnetoelectric (ME) effect. The exchange striction mechanism explains the remarkable ME response in the two sublattice type-I multiferroic materials. These results and their interpretation demonstrate a method for realizing multistage magnetoelectric effects in hybrid spin systems.

DOI: [10.1103/PhysRevB.109.094419](https://doi.org/10.1103/PhysRevB.109.094419)

I. INTRODUCTION

In recent years, the rapid development of information technologies has driven the search for new materials and mechanisms for electronic devices. In particular, “multiferroic” materials, which were first discovered over half a century ago [1,2], have become a promising candidate for future low-power memory devices. The industrial demands have resulted in increasing scientific and industrial interest in “multiferroics” since 2000 [3–8]. The prominent magnetoelectric (ME) effect in TbMnO_3 revealed type-II multiferroic materials in which the ferroelectricity originates from their magnetic order [9]. However, recent studies revealed that magnetic transitions in type-I multiferroic materials, in which the ferroelectricity or polarity is of a different origin from the magnetism, can also have a significant ME effect [10].

The honeycomb magnet $\text{Fe}_2\text{Mo}_3\text{O}_8$, one of the type-I multiferroic materials, belongs to the family of ternary transition-metal molybdenum oxides, and it possesses a polar hexagonal structure (pyroelectric space-group $P-6_3mc$) [11] with c -axis crystallographic polarity. In $\text{Fe}_2\text{Mo}_3\text{O}_8$, the Fe^{2+} ions are located in tetrahedrally coordinated sites (A-sites) as well as in octahedrally coordinated sites (B-sites) of oxygen, and they are interleaved in the ab plane to form honeycomb layers [Fig. 1(a)]. The Mo^{4+} ions form nonmagnetic spin-singlet trimers [12] and separate each Fe^{2+} honeycomb layer along the c axis. The A and B sites on adjacent layers occupy opposite positions. Below a Néel temperature of 60 K, the spins of the Fe^{2+} ions ($S = 2$) are aligned in a collinear antiferromagnetic (AFM) order [13]. In this AFM state, the spins in the nearest interplane A-B sites point in the same direction, whereas those in the nearest intraplane A-B sites take opposite orientations [Fig. 1(b)]. Early studies claimed the larger magnetic moments with strong Ising anisotropy for

the octahedral B sites [14], while recent studies proposed the larger anisotropic moments in the A sites [15]. Although this paper follows the latter interpretation, i.e., $m_A > m_B$, it does not affect the essential points of the discussion. Because of the difference in the magnetic moments, the application of the magnetic fields along the polar axis stabilizes the ferrimagnetic (FiM) state. In this FiM state, all the spins of the A and B sites are aligned parallel and antiparallel to the magnetic field, respectively. The competition between the AFM and FiM orders can be finely tuned by chemical doping [14]. $\text{Fe}_2\text{Mo}_3\text{O}_8$ and its Zn-doped compounds exhibit a linear ME [16], optical ME [17], electromagnon excitations [18], and significant thermal Hall effects [19]. In addition, the giant ME response [16,20] reveals the nature of the exchange-striction mechanism [21].

In this study, we investigate the high-field properties of the honeycomb polar magnet $\text{Fe}_2\text{Mo}_3\text{O}_8$. Multistep magnetization and the corresponding giant ME responses are observed at low temperatures when a magnetic field is applied along the polar axis. We interpret the experimental findings using a combined triangular lattice model with Ising-type anisotropy and the exchange-striction mechanism.

II. EXPERIMENTAL

Single crystals of $\text{Fe}_2\text{Mo}_3\text{O}_8$ (samples K1, K2, and K3) were grown by the chemical vapor transport method [22]. The crystal orientations were confirmed using x-ray Laue diffraction measurements. Pulsed-magnetic fields of up to 66 T with durations of 4–36 ms were generated by several types of nondestructive pulse magnets provided by the International MegaGauss Science Laboratory at the Institute for Solid State Physics, the University of Tokyo. The magnetization (M) in pulsed-fields was measured using the conventional induction

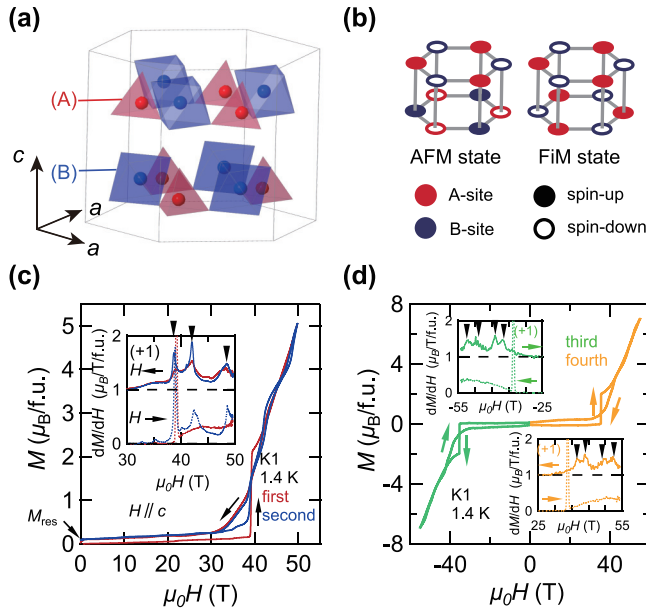


FIG. 1. (a) Schematic arrangement of FeO_4 and FeO_6 in a magnetic unit cell of $\text{Fe}_2\text{Mo}_3\text{O}_8$. The red and blue circles represent Fe ions in the A- and B-sites, respectively. (b) Schematic of the AFM and FiM states. (c) Virgin (red) and secondary (blue) magnetization curves of $\text{Fe}_2\text{Mo}_3\text{O}_8$ at 1.4 K in a pulsed magnetic field (durations of 10 ms) applied along the polar axis. (d) Magnetization curves after reversing the polarity of magnetic fields (durations of 36 ms). The insets in (c) and (d) show the field derivative of the magnetization curves with corresponding colors.

method with coaxial pick-up coils. The absolute value of the magnetization was calibrated by magnetization measurements using a commercial superconducting quantum interference device magnetometer system (MPMS; Quantum Design). The relative change in electric polarization (ΔP) with respect to the initial values at zero field was measured by integrating the polarization currents induced by the magnetic fields [23]. The electrodes were constructed using gold wires with carbon-based paste painted on two flat surfaces perpendicular to the c axis. The sign of the polarization taken from [16] is defined as the spin-driven contribution appearing negative below 60 K. The extrinsic background caused by the large time-derivative of the magnetic fields was evaluated by reversing the polarity of the magnetic fields above the Néel temperature and removed from all the data.

III. RESULTS AND DISCUSSION

As shown in Fig. 1(c), we measured the magnetization of $\text{Fe}_2\text{Mo}_3\text{O}_8$ in pulsed magnetic fields along the c axis at 1.4 K. The magnetization increases steeply at approximately 40 T during the field-increasing process of the virgin trace. Although there was a relatively smooth change in the further field-increasing process of the virgin trace, a clear wiggling behavior emerged in the field-decreasing process and the secondary trace. In the field-derivative curve panel (inset), we obtained three peak structures at approximately 39, 41, and 48 T below 50 T as marked by black triangles. A finite residual magnetic moment (M_{res}) exists in the virgin cycle at this temperature when the magnetic field decreases to zero. From the

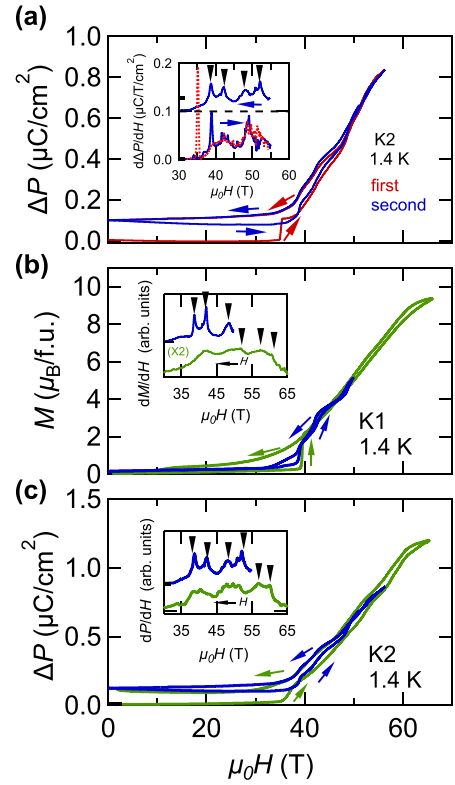


FIG. 2. (a) Virgin (red) and secondary (blue) electric polarization curves of $\text{Fe}_2\text{Mo}_3\text{O}_8$ at 1.4 K in a pulsed magnetic field (durations of 36 ms) applied along the polar axis. (b) Magnetization in magnetic fields of up to 66 (green) and 50 T (blue). (c) Electric polarization in magnetic fields of up to 66 (green) and 56 T (blue). The insets show the field derivative of the magnetization and electric polarization curves with corresponding colors in the field-decreasing process.

secondary measurements, the magnetization curves exhibit wiggling behaviors in both field-increasing and -decreasing processes while maintaining this temperature. Upon application of a negative field afterward, the M - H curve becomes similar to that in the first field-sweep process. We observed wiggling traces after a smooth change in the field-increasing process as shown in Fig. 1(d). When the magnetic field direction is reversed, the magnetization exhibits an antisymmetric character.

Next, we measured the field-induced change in electric polarization along the c axis at 1.4 K [Fig. 2(a)]. History-dependent multistep behavior was also observed in the P - H curves. The P - H profiles in the field-increasing process of the virgin trace is relatively smooth, similar to the case of the M - H measurements. In the inset of Fig. 2(a), four peak structures are observed in the field derivative curves below 55 T. Here, the zero point of ΔP is defined by the initial value of the electric polarization in the virgin trace.

To clarify the behavior up to the saturation field above 60 T, we measured the magnetization and electric polarization using a short-pulse magnet (with a duration of 4 ms). As indicated by the green curve in Fig. 2(b), the magnetization reaches approximately $9.2 \mu_B/\text{f.u.}$ at 66 T, which is close to the expected saturation moment of the material. In this fully spin-polarized (FSP) state, all the spins of the A- and B-site

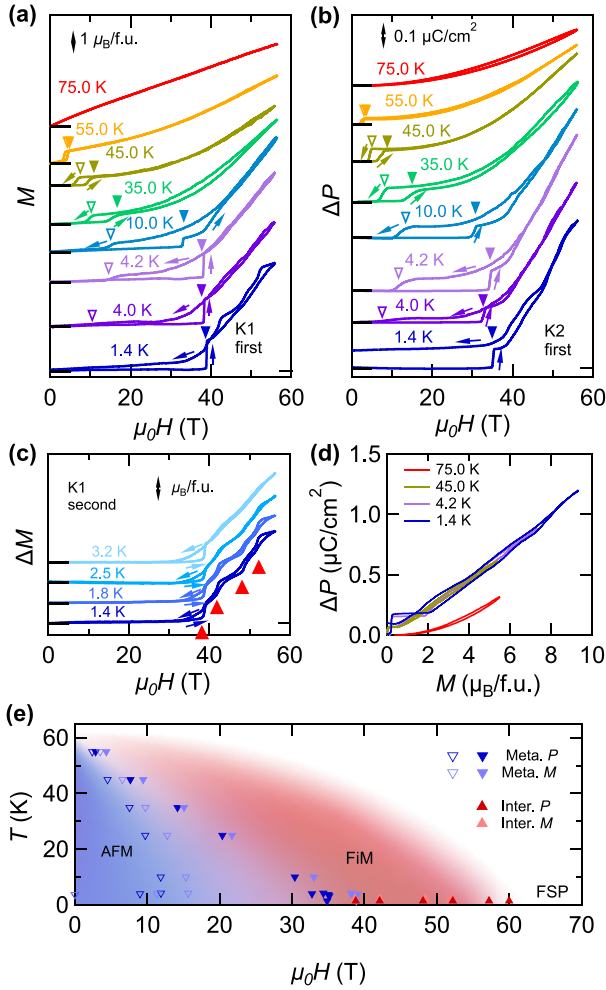


FIG. 3. Magnetic field dependence of (a) M and (b) ΔP at various temperatures. The data were vertically offset for clarity. (c) Temperature dependence of multistep structures in magnetization below 3.2 K. ΔM here denotes the relative change in the magnetization from zero field, as there are finite residual magnetic moments in the secondary curves. (d) Relationship between ΔP and M at different temperatures. (e) Magnetic phase diagram in the T - H plane. The closed (open) inverted triangles represent critical fields of AFM \rightarrow FiM (FiM \rightarrow AFM) transitions. The red triangles represent peak fields in the dM/dH and dP/dH curves. The Meta. P (M) and Inter. P (M) denote the transition fields between AFM and FiM states, and the transition fields between intermediate states in the P (M) curves, respectively.

iron ions align parallel to the magnetic field. Moreover, the total change in the electric polarization amounts to $1.2 \mu\text{C}/\text{cm}^2$ at 66 T, as shown in Fig. 2(c). From the derivative curves of the field-decreasing process, we obtained six peak structures between 35 and 65 T (insets). The field positions of the peaks between the polarization and magnetization measurements al-

most coincide. Nevertheless, the peaks are more prominent in midpulse magnets [Figs. 1(c) and 2(a), duration of 10–36 ms]; therefore, it takes sufficient time to stabilize the intermediate states discussed later.

We also investigated the field dependence of the magnetization and polarization at various temperatures [Figs. 3(a) and 3(b)]. The field at the first steep increase in M and ΔP shifted to a lower value with increasing temperature and merged with the reported transition fields from the AFM state to the FiM state at high temperatures [16]. Therefore, we attribute all the anomalies marked by triangles to transitions between the AFM and FiM states. Below approximately 4 K, we observed a finite residual magnetic moment and electric polarization as the magnetic field returned to zero. In addition, the wiggling behavior gradually blurred with increasing temperature and was barely visible at 3.2 K, as shown in Fig. 3(c). In Fig. 3(d), the ΔP change linearly with the M below the Néel temperature of 60 K. In the paramagnetic region, ΔP is proportional to the square of M ; see the red curve at 75 K in Fig. 3(d). We plotted the peak positions of the dM/dH and dP/dH curves in the temperature-field plane [Fig. 3(e)]. The multistep behavior only appears when the remnant FiM state exists below approximately 3 K. Although there is a finite discrepancy in the transition field between the AFM and FiM phases determined by P (sample K2) and M (sample K1) at low temperatures, we confirmed that this discrepancy originates from the slight sample dependence. Simultaneous measurements of M and ΔP in one sample (K3) confirmed their coincidence at 1.4 K [24]. The multistep behaviors in the K1 and K2 samples also appear at the same field positions. However, we were unable to detect any feature of this multistep behavior in Mn-doped $\text{Fe}_2\text{Mo}_3\text{O}_8$ [24].

In the following, we discuss the origin of the observed multistep magnetization process. As mentioned earlier, we consider a phase transition from the AFM state to the FiM state at the first magnetization step. The FSP state is realized under a magnetic field of 66 T. Figures 4(a) and 4(b) schematically show the respective spin configurations in these states. The red and blue circles denote the A- and B-site ions, respectively, and the open and closed circles represent down and up spins, respectively. In both states, the A-site spins align parallel to the magnetic field, whereas the B-site spins are antiparallel and parallel in the FiM and FSP states, respectively. Our experimental results suggest the emergence of five intermediate states during the reorientation of the B-site spins.

If we consider only the B-site spins, they form a triangular lattice in the ab plane. The magnetization processes of triangular lattice antiferromagnets are usually expressed by three magnetic sublattices. Because the crystallographic unit cell of the present material contains ions in adjacent layers, we consider six magnetic sublattices for both the A- and B-site spins. Considering its strong Ising-type nature [25], we express the spin Hamiltonian of this material as

$$\begin{aligned} \mathcal{H} = & -J_1 \sum_{i \in B} s_i (\sigma_{i+e_1} + \sigma_{i+e_2} + \sigma_{i+e_3}) - J_{AB} \sum_{i \in B} s_i (\sigma_{i-c} + \sigma_{i+c}) \\ & - J_{BB} \sum_{i \in B} s_i (s_{i+e_1+c} + s_{i+e_2+c} + s_{i+e_3+c}) - J_{AA} \sum_{i \in A} \sigma_i (\sigma_{i+e_1+c} + \sigma_{i+e_2+c} + \sigma_{i+e_3+c}) \end{aligned}$$

$$\begin{aligned}
& -J_{2B} \sum_{i \in B} s_i (s_{i+a_1} + s_{i+a_2} + s_{i+a_3}) - J_{2A} \sum_{i \in A} \sigma_i (\sigma_{i+a_1} + \sigma_{i+a_2} + \sigma_{i+a_3}) \\
& - \mu_0 H \left(\sum_{i \in B} m_B s_i + \sum_{i \in A} m_A \sigma_i \right), \tag{1}
\end{aligned}$$

where $s_i, \sigma_i = \pm 1$ denote the normalized Ising variables of the B- and A-site iron spins, whereas m_A and m_B represent the magnitude of the moments, respectively. Here, e_n, a_n, c describe the relative locations of the nearest intraplane neighbor sites, the second nearest intraplane neighbor sites, and the nearest interplane neighbor sites, respectively [Figs. 4(c) and 4(d)]. Here, we consider the exchange interactions between the nearest intraplane A-B sites (J_1), the nearest interplane A-B sites (J_{AB}), the second nearest intraplane A-A sites (J_{2A}), the second nearest intraplane B-B sites (J_{2B}), the nearest interplane A-A sites (J_{AA}), and the nearest interplane B-B sites (J_{BB}) together with the Zeeman term.

Let us consider the sequential spin-flipping process from the AFM state to the FSP state. Here, we label the state as Nn , where the integer $n = 0 - 6$ represents the number of up-spins in the six magnetic sublattices in the B-sites, that is, N0 and N6 for the FiM and FSP states, respectively. As an example, in Figs. 4(c) and 4(d), we illustrate intraplane and interplane spin configurations in the N1 state. Sequential transition can be reproduced by choosing the appropriate parameters for this Hamiltonian. In this model, the magnitude of magnetization in the Nn state is given by

$$M_{Nn} = m_A - \left(1 - \frac{n}{3}\right)m_B. \tag{2}$$

From the M - H curves at 1.4 K, we determined the magnetic moments $m_A = 4.9 \pm 0.25 \mu_B/\text{Fe}$ and $m_B = 4.3 \pm 0.22 \mu_B/\text{Fe}$. Using the reported value of $J_{AB} = 0.100$ meV [25], we determined the other parameters as $J_1 = -4.2 \pm 0.2$ meV, $J_{BB} = -0.15 \pm 0.007$ meV, $J_{AA} = 0.07 \pm 0.003$ meV, and $J_{2B} = -0.26 \pm 0.017$ meV. Here, we cannot fix the value of J_{2A} because it only causes identical energy shifts for all states considered. The details of the calculations are described in the supplemental material [24]. As shown in Fig. 1(c), the steep jump in the initial magnetization process of the K1 sample takes place at 39 T with a jump height of $2\mu_B/\text{Fe}$, which is different from the K2 and K3 samples. We consider the state of the K1 sample above the transition field as almost the N1 state with a magnetic moment of $m_A - 2/3m_B = 2 \mu_B/\text{Fe}$. Since the energies of the N0 and N1 states are almost degenerated at this field, some of the magnetic moments of the B-site spins can be trapped in the local energy minima state during the fast field sweep at low temperatures.

Here, we note the multiple possible spin configurations in the N2, N3, and N4 states. If we express the spin configuration by $(\text{sgn}(s_1), \text{sgn}(s_2), \text{sgn}(s_3))/(\text{sgn}(s_4), \text{sgn}(s_5), \text{sgn}(s_6))$, two N2 states $(-, -, +)/(-, -, +)$ and $(+, +, -)/(-, -, -)$ have different energies. For the parameters that

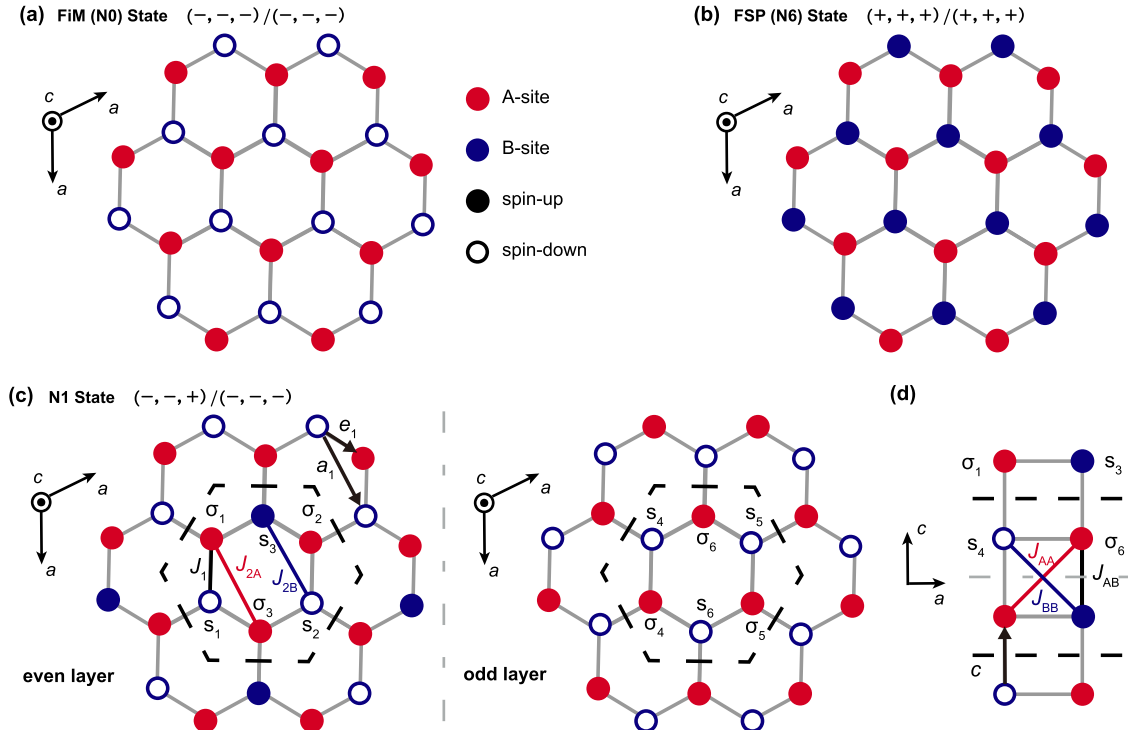


FIG. 4. (a), (b) Schematic illustrations of the FiM and FSP states in the ab plane, respectively. (c), (d) Schematic illustrations of the N1 state projected on the ab and ac planes, respectively. The thick broken lines represents the boundaries in magnetic unit cells.

reproduce the multistep M - H curve, we found the lowest energy states for N2, N3, and N4 states to be $(-, -, +)/(-, -, +)$, $(+, +, -)/(-, -, +)$, and $(+, +, -)/(+, +, -)$, respectively. Notably, there are other states including four or two B-site sublattices states in one magnetic unit cell. We can rule out this four-sublattice state by considering the frustration in the exchange striction effect around the B-site ions [24].

Next, we focus on the ME effect. The ME effect at low fields in this material was explained by the g -factor mechanism [16]. To reproduce the ME effects observed in the FiM states using a similar quadratic function of the magnetic field, we have to introduce an unnatural temperature dependence of the coefficients. The g -factor model may explain the ME effect at low fields, as seen below 40 T in Fig. 2(a), but we discuss the other origin for the gigantic ME effects observed in the FiM states below. Among the three major mechanisms [26], we can rule out the inverse Dzyaloshinskii-Moriya interaction because of the collinear spin configuration in the present material. In addition, the p - d hybridization mechanism may not be relevant because a 180° spin-flip does not cause any change in the electric polarization in this mechanism. Therefore, we consider the exchange striction mechanism [27] to describe the ME coupling in $\text{Fe}_2\text{Mo}_3\text{O}_8$.

Here, we express the electrical polarization caused by the exchange striction mechanism using the following equation:

$$P^c = \frac{1}{V} \left[\sum_{i \in B} \Pi_{\parallel} s_i (\sigma_{i+e_1} + \sigma_{i+e_2} + \sigma_{i+e_3}) + \sum_{i \in B} (\Pi_{\perp}^+ s_i \sigma_{i+c/2} + \Pi_{\perp}^- s_i \sigma_{i-c/2}) \right], \quad (3)$$

where V is the volume of the crystallographic unit cell, and Π_{\parallel} and Π_{\perp}^{\pm} denote contributions from the adjacent intraplane and interplane AB spin arrangements, respectively. We distinguish between Π_{\parallel} and Π_{\perp}^{\pm} by noting that the tetrahedron is asymmetric at the top and bottom. Using this model, the electric polarization changes by $2(\Pi_{\perp}^+ + \Pi_{\perp}^-)$ per B-site in the transition from the AFM to the FiM phase and by $6\Pi_{\parallel}$ to the FSP phase. As shown in Fig. 2(c), the latter is ten times larger in the experiment, indicating that the intraplane contribution to the change in electric polarization is dominant. When A-sublattice spins are fixed to the direction of the external magnetic field, $\sigma_i = 1$, the electric polarization in Eq. (3) is proportional to the magnetization at the B-sublattice, $P^c \propto \sum (3\Pi_{\parallel} + \Pi_{\perp}^+ + \Pi_{\perp}^-) s_i$. Such a relationship is consistent with the experimental observation at low temperatures shown in Fig. 2(d).

The solid blue lines in Figs. 5(a) and 5(b) show the field dependence of magnetization and electric polarization calculated for multistep spin configurations in Fig. 5(a) using Eqs. (2) and (3). The red and green dashed lines in the figure are the corresponding experimental results. Since the three parameters in Eq. (3) cannot be determined independently from the information obtained in this experiment, we tentatively use $\Pi_{\parallel} = 2.7 \times 10^{-31}$ C m, $\Pi_{\perp}^+ + \Pi_{\perp}^- = -7.2 \times 10^{-32}$ C m. As can be seen in the figure, the experimental and theoretical results are generally in good agreement, suggesting the validity of the model. In particular, the locations of the

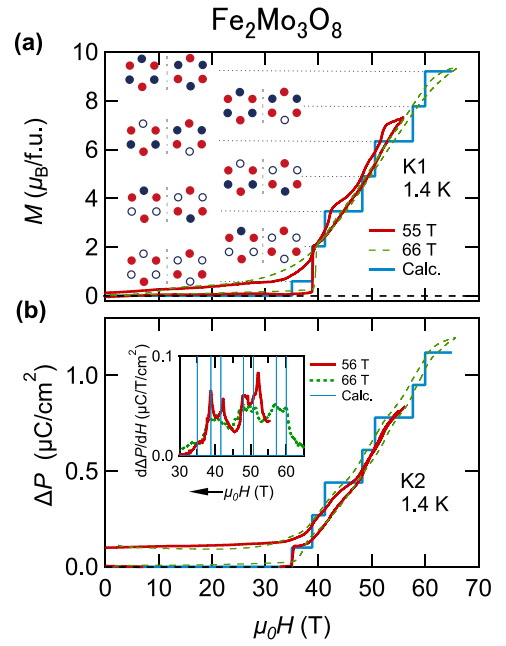


FIG. 5. Comparison between the experimental (red, green) and calculated (blue) curves of (a) M and (b) ΔP . Here, ΔP represents the change from the AFM state. The inset in (b) shows the field derivative of experimental and calculated electric polarization curves. The black arrow indicates that the field derivative curves in the inset are derived from the field-decreasing process.

transition fields are reasonably reproduced using the present parameters, as shown in the inset of Fig. 5(b).

Let us consider why we do not observe the multistep M - H and P - H profiles in the initial field ramp-up process. In this process, the transition from the AFM to the N0 state requires spin flips for half of the spins in the B sites. Since the energy of each plateau state almost degenerated, as seen in Fig. S2, some of the spins can be trapped in the intermediate states in the fast field sweep. A similar situation takes place when we invert the field direction. In this case, we must flip all the B-site spins at the transition from the N0 state in the positive field to that in the negative field. The partial existence of nonequilibrium states can suppress the plateau state. The direct transition from the AFM to N1 state in the virgin trace of the K1 sample also suggests the existence of energy-trapping during the fast field sweep. This significant magnetization change is a nonequilibrium phenomenon due to the nucleation process in the first-order transition.

Several recent studies revealed high-field properties of the related molybdates $\text{Ni}_2\text{Mo}_3\text{O}_8$ [28] and $\text{Co}_2\text{Mo}_3\text{O}_8$ [29,30]. Due to the weaker spin anisotropy, applying high magnetic fields along the c axis causes spin-flop and stabilizes canted spin states in these materials. Strong spin anisotropy in $\text{Fe}_2\text{Mo}_3\text{O}_8$ originated from strong spin-lattice coupling realizes unusual multistep magnetoelectric plateaus and three to five times larger change in the electric polarization by the transition from the AFM to FSP state.

Multiple magnetization plateaus have been previously observed in a triangular-lattice Ising spin system $\text{Ca}_3\text{Co}_2\text{O}_6$ [31]. The steplike structures in $\text{Ca}_3\text{Co}_2\text{O}_6$ gradually vanish as the sweep rate decreases. This result indicates that the

multiple magnetization plateaus in this material are related to a nonequilibrium process, except for the 1/3 one. On the contrary, the multistep magnetization in $\text{Fe}_2\text{Mo}_3\text{O}_8$ becomes more evident at a slower sweeping rate, as shown in Figs. 2(b) and 2(c), which suggests the existence of the equilibrium intermediate states.

Recently, we noticed that Chang *et al.* reported the M - H and P - H curves on this material [32]. Contrary to our results, they did not observe multistep behavior and explained their magnetization process assuming easy-plane-type spin anisotropy for the B sites. The origin of this discrepancy is unclear to us because they showed neither the M - H curves in the field ramp-down process nor the differential magnetization curves.

Our findings of simultaneously discretized M - H and P - H curves suggest a novel control method for frustrated magnets. At a magnetic field between two plateau states, we can expect switching between the two plateau states by applying electric fields. Such an electric control of the magnon superlattice will be an interesting challenge in future studies.

In type-II multiferroic materials, magnetic order that breaks spatial inversion symmetry is essential to generate

electric polarization. However, type-I multiferroic materials, which do not have inversion symmetry even in a paramagnetic state, can host the magnetoelectric effect without symmetry-lowering of the magnetic order. As in the present material, the electric polarization originating from the exchange striction mechanism can be inverted between parallel and antiparallel spin configurations. Since exchange striction mechanisms are known to cause significant magnetoelectric effects, our results reveal the application potential (for magnetic sensor, data storage, etc.) of type-I multiferroic materials.

IV. SUMMARY

In summary, we report unusual multistep magnetization and the corresponding giant magnetoelectric effect in single-crystalline $\text{Fe}_2\text{Mo}_3\text{O}_8$. A fully spin-polarized state was realized in this system in magnetic fields of up to 66 T applied along the polar axis at 1.4 K. This six-step magnetization and ME processes are unique to this material and is interpreted using a combined triangular lattice model with strong Ising-type anisotropy. The exchange striction mechanism reasonably reproduces the corresponding multistep electric polarization.

-
- [1] I. E. Dzyaloshinskii, On the magneto-electrical effects in anti-ferromagnets, *Sov. Phys. JETP* **10**, 628 (1960).
- [2] D. Astrov, The magnetoelectric effect in antiferromagnetics, *Sov. Phys. JETP* **11**, 708 (1960).
- [3] H. Schmid, Introduction to the proceedings of the 2nd international conference on magnetoelectric interaction phenomena in crystals, MEIPIC-2, *Ferroelectrics* **161**, 1 (1994).
- [4] N. A. Hill, Why are there so few magnetic ferroelectrics? *J. Phys. Chem. B* **104**, 6694 (2000).
- [5] W. Eerenstein, N. Mathur, and J. F. Scott, Multiferroic and magnetoelectric materials, *Nature (London)* **442**, 759 (2006).
- [6] Y. Tokura, Multiferroics—toward strong coupling between magnetization and polarization in a solid, *J. Magn. Magn. Mater.* **310**, 1145 (2007).
- [7] Y. Tokura and S. Seki, Multiferroics with spiral spin orders, *Adv. Mater.* **22**, 1554 (2010).
- [8] M. M. Vopson, Fundamentals of multiferroic materials and their possible applications, *Crit. Rev. Solid State Mater. Sci.* **40**, 223 (2015).
- [9] T. Kimura, T. Goto, H. Shintani, K. Ishizaka, T.-H. Arima, and Y. Tokura, Magnetic control of ferroelectric polarization, *Nature (London)* **426**, 55 (2003).
- [10] J. Dho, X. Qi, H. Kim, J. L. MacManus-Driscoll, and M. G. Blamire, Large electric polarization and exchange bias in multiferroic BiFeO_3 , *Adv. Mater.* **18**, 1445 (2006).
- [11] W. H. McCarrroll, L. Katz, and R. Ward, Some ternary oxides of tetravalent molybdenum^{1,2}, *J. Am. Chem. Soc.* **79**, 5410 (1957).
- [12] F. A. Cotton, Metal atom clusters in oxide systems, *Inorg. Chem.* **3**, 1217 (1964).
- [13] S. McAlister and P. Strobel, Magnetic order in $\text{M}_2\text{Mo}_3\text{O}_8$ single crystals ($M = \text{Mn, Fe, Co, Ni}$), *J. Magn. Magn. Mater.* **30**, 340 (1983).
- [14] D. Bertrand and H. Kerner-Czeskleba, Structural and magnetic study of iron-group molybdates, *J. Phys. France* **36**, 379 (1975).
- [15] S. Reschke, A. A. Tsirlin, N. Khan, L. Prodan, V. Tsurkan, I. Kezsmarki, and J. Deisenhofer, Structure, phonons, and orbital degrees of freedom in $\text{Fe}_2\text{Mo}_3\text{O}_8$, *Phys. Rev. B* **102**, 094307 (2020).
- [16] T. Kurumaji, S. Ishiwata, and Y. Tokura, Doping-tunable ferrimagnetic phase with large linear magnetoelectric effect in a polar magnet $\text{Fe}_2\text{Mo}_3\text{O}_8$, *Phys. Rev. X* **5**, 031034 (2015).
- [17] T. Kurumaji, Y. Takahashi, J. Fujioka, R. Masuda, H. Shishikura, S. Ishiwata, and Y. Tokura, Optical magnetoelectric resonance in a polar magnet $(\text{Fe, Zn})_2\text{Mo}_3\text{O}_8$ with axion-type coupling, *Phys. Rev. Lett.* **119**, 077206 (2017).
- [18] T. Kurumaji, Y. Takahashi, J. Fujioka, R. Masuda, H. Shishikura, S. Ishiwata, and Y. Tokura, Electromagnon resonance in a collinear spin state of the polar antiferromagnet $\text{Fe}_2\text{Mo}_3\text{O}_8$, *Phys. Rev. B* **95**, 020405(R) (2017).
- [19] T. Ideue, T. Kurumaji, S. Ishiwata, and Y. Tokura, Giant thermal Hall effect in multiferroics, *Nat. Mater.* **16**, 797 (2017).
- [20] Y. Wang, G. L. Pascut, B. Gao, T. A. Tyson, K. Haule, V. Kiryukhin, and S.-W. Cheong, Unveiling hidden ferrimagnetism and giant magnetoelectricity in polar magnet $\text{Fe}_2\text{Mo}_3\text{O}_8$, *Sci. Rep.* **5**, 12268 (2015).
- [21] T.-H. Arima, Ferroelectricity induced by proper-screw type magnetic order, *J. Phys. Soc. Jpn.* **76**, 073702 (2007).
- [22] P. Strobel and Y. Le Page, Growth and morphology of single crystals of hexagonal molybdates (iv) $\text{M}_2\text{Mo}_3\text{O}_8$ ($M = \text{Mn, Fe, Co, Ni}$), *J. Cryst. Growth* **61**, 329 (1983).
- [23] H. Mitamura, S. Mitsuda, S. Kanetsuki, H. Aruga Katori, T. Sakakibara, and K. Kindo, Dielectric polarization measurements on the antiferromagnetic triangular lattice system CuFeO_2 in pulsed high magnetic fields, *J. Phys. Soc. Jpn.* **76**, 094709 (2007).
- [24] See Supplemental Material at <http://link.aps.org/supplemental/10.1103/PhysRevB.109.094419> for the simultaneous measure-

- ments of M and δP in the k3 sample (S1), the energy estimation for each magnetic state (S2), the existence of the other spin configurations (S3), and the magnetization in Mn-doped $\text{Fe}_2\text{Mo}_3\text{O}_8$ (S4). It also contains Ref. [25].
- [25] S. Ghara, E. Barts, K. Vasin, D. Kamenskyi, L. Prodan, V. Tsurkan, I. Kézsmárki, M. Mostovoy, and J. Deisenhofer, Magnetization reversal through an antiferromagnetic state, *Nat. Commun.* **14**, 5174 (2023).
- [26] Y. Tokura, S. Seki, and N. Nagaosa, Multiferroics of spin origin, *Rep. Prog. Phys.* **77**, 076501 (2014).
- [27] I. A. Sergienko, C. Şen, and E. Dagotto, Ferroelectricity in the magnetic E -phase of orthorhombic perovskites, *Phys. Rev. Lett.* **97**, 227204 (2006).
- [28] Y. Tang, J. Zhang, L. Lin, R. Chen, J. Wang, S. Zheng, C. Li, Y. Zhang, G. Zhou, L. Huang *et al.*, Metamagnetic transitions and magnetoelectricity in the spin-1 honeycomb antiferromagnet $\text{Ni}_2\text{Mo}_3\text{O}_8$, *Phys. Rev. B* **103**, 014112 (2021).
- [29] D. Szaller, L. Prodan, K. Geirhos, V. Felea, Y. Skourski, D. Gorbunov, T. Förster, T. Helm, T. Nomura, A. Miyata *et al.*, Coexistence of antiferromagnetism and ferrimagnetism in adjacent honeycomb layers, [arXiv:2202.04700](https://arxiv.org/abs/2202.04700) (2022).
- [30] Y. Tang, G. Zhou, L. Lin, R. Chen, J. Wang, C. Lu, L. Huang, J. Zhang, Z. Yan, X. Lu *et al.*, Successive electric polarization transitions induced by high magnetic field in the single-crystal antiferromagnet $\text{Co}_2\text{Mo}_3\text{O}_8$, *Phys. Rev. B* **105**, 064108 (2022).
- [31] V. Hardy, M. Lees, O. A. Petrenko, D. Mck. Paul, D. Flahaut, S. Hébert, and A. Maignan, Temperature and time dependence of the field-driven magnetization steps in $\text{Ca}_3\text{Co}_2\text{O}_6$ single crystals, *Phys. Rev. B* **70**, 064424 (2004).
- [32] Y. Chang, Y. Weng, Y. Xie, B. You, J. Wang, L. Li, J.-M. Liu, S. Dong, and C. Lu, Colossal linear magnetoelectricity in polar magnet $\text{Fe}_2\text{Mo}_3\text{O}_8$, *Phys. Rev. Lett.* **131**, 136701 (2023).